

PAPER • OPEN ACCESS

Robust thermal control for CMOS-based lab-on-chip systems

To cite this article: Jose Martinez-Quijada *et al* 2015 *J. Micromech. Microeng.* **25** 075005

View the [article online](#) for updates and enhancements.

You may also like

- [The emergence of 3D bioprinting in organ-on-chip systems](#)
Kirsten Fetah, Peyton Tebon, Marcus J Goudie et al.
- [3D-printed microfluidic devices](#)
Reza Amin, Stephanie Knowlton, Alexander Hart et al.
- [A novel concept for long-term pre-storage and release of liquids for pressure-driven lab-on-a-chip devices](#)
D Czurratis, Y Beyl, S Zinober et al.

Robust thermal control for CMOS-based lab-on-chip systems

Jose Martinez-Quijada¹, Tianchi Ma², Gordon H Hall², Matt Reynolds¹,
David Sloan¹, Saul Caverhill-Godkewitsch¹, D Moira Glerum³,
Dan Sameoto⁴, Duncan G Elliott¹ and Christopher J Backhouse²

¹ Electrical and Computer Engineering Dept., University of Alberta, Edmonton, Alberta, Canada

² Electrical and Computer Engineering Dept., University of Waterloo, Waterloo, Ontario, Canada

³ Biology Dept., University of Waterloo, 200 University Avenue West, Waterloo, Ontario, N2L 3G1, Canada

⁴ Mechanical Engineering Dept., University of Alberta, Edmonton, Alberta, Canada

E-mail: chrisb@uwaterloo.ca

Received 29 December 2014, revised 24 March 2015

Accepted for publication 21 April 2015

Published 22 May 2015



CrossMark

Abstract

The need for precise temperature control at small scales has provided a formidable challenge to the lab-on-chip community. It requires, at once, good thermal conductivity for high speed operation, good thermal isolation for low power consumption and the ability to have small (mm-scale) thermally independent regions on the same substrate. Most importantly, and, in addition to these conflicting requirements, there is a need to accurately measure the temperature of the active region without the need for device-to-device calibrations. We have developed and tested a design that enables thermal control of lab-on-chip devices atop silicon substrates in a way that could be integrated with the standard methods of mass-manufacture used in the electronics industry (i.e. CMOS). This is a significant step towards a single-chip lab-on-chip solution, one in which the microfluidics, high voltage electronics, optoelectronics, instrumentation electronics, and the world-chip interface are all integrated on a single substrate with multiple, independent, thermally-controlled regions based on active heating and passive cooling.

Keywords: BioMEMS, lab-on-chip, microthermal, microfluidics


(Some figures may appear in colour only in the online journal)

1. Introduction

A central challenge for the development of the lab-on-chip technologies is that of integrating rapid and precise temperature control over small localised regions in a way that lends itself to mass-manufacture and point-of-care applications. An ideal implementation would use resistive heating and passive cooling and be compatible with CMOS electronics, the standard micro and nanoelectronic technology based on silicon. However, this is a challenging optimisation problem requiring enough thermal isolation to have reasonably low power

requirements (i.e. Watts or less). In addition, sufficient thermal conductivity is needed for rapid cooling for lab-on-chip protocols, such as the polymerase chain reaction (PCR), with time constants of less than a minute. Any design also needs to be small enough to allow several temperature-controlled regions on a standard CMOS chip substrate (i.e. the millimeter scale). Most importantly, the design must minimise the effects of poorly controlled boundary conditions (such as air temperature and velocity) in order to allow for reproducible thermal control without the need for extensive instrumentation and calibrations (device-level or run-time) that are incompatible with point-of-care use.

Considerable effort has been expended to improve the thermal control on lab-on-chip systems. In their review, Jain and Goodson [1] note that thermal control is centrally

 Content from this work may be used under the terms of the [Creative Commons Attribution 3.0 licence](https://creativecommons.org/licenses/by/3.0/). Any further distribution of this work must maintain attribution to the author(s) and the title of the work, journal citation and DOI.

important for a wide range of BioMEMS implementations. Ahmad and Hashsham [2] recently presented a survey of miniaturised thermal systems for genetic analysis while the review by Saha and Chaudhuri [3] provides a good overview of the state of CMOS/MEMS integrations. As noted by Ahmad and Hashsham, the verification of temperature uniformity is a challenge, often calling for calibration runs or the use of sensors that perturb the temperature distribution. In order to allow for thermally independent regions within a heated silicon system, some have made use of micromachined trenches for thermal isolation. However, such micromachining is not readily compatible with CMOS manufacture and calibration remains a problem.

One might think that this problem has long since been solved by the remarkable tour-de-force of Burns *et al* [4] (of over a decade ago) with their integration of heaters and sensors in a pneumatically and electrically actuated system for integrated genetic amplification and electrophoretic separation. However, the drawback of their system was that it contained heaters essentially atop the silicon itself and as such would tend to run the entire chip at the same temperature. Although it could be heated rapidly (up to $10 \frac{C}{s}$), it would likely cool slowly given the large thermal mass of the system. The cooling time was of little consequence for their largely isothermal application, but would complicate, if not preclude, more dynamic applications such as PCR (in its many forms). Even more importantly, the use of unisolated, high thermal conductivity materials such as silicon would lead to large temperature differences that could cause problematic calibration requirements at the time of use. Moreover, although their design was small enough to be cost-effective for simple silicon-based electronics (e.g. diodes and metallisation) it was too large to be cost-effective for a full CMOS technology. This is not to detract from that landmark in the field, but many of the challenges from that time are still with us.

This has long been an active area of development for silicon or CMOS-based integration, with the work of Baltes *et al* [5] and others (e.g. [6–8]) being representative of one of the main approaches: the use of micromachined or membrane-based heaters for low-power (e.g. a few tens of mW). Although the membrane gives so much isolation that low power operation is enabled, it can also render the isolated region very susceptible to changes in heat loss, notably by means of air conduction and convection. Since these effects can vary significantly, this results in a loss of stability against perturbations.

Other approaches (Hoang *et al* [9], Selva *et al* [10] or Furuhashi *et al* [11]) do not require such isolation (or substantial removal of substrate material), but make the active region tightly coupled to the local environment, requiring additional instrumentation (e.g. measuring local temperatures) and, (most importantly) typically requiring calibrations of each device prior to running. Such calibrations are crucial given that the sensor temperature may differ by several to tens of degrees C from that of the region of interest (typically a microscale chamber). However, as noted by [12], and as used by us previously, the heater can also be used as a sensor and so can be very closely coupled with the chamber, which could give a very accurate readout of the chamber temperature.

More recently, Jung *et al* [13] presented Pt/Ti heaters on silicon that were coated with a thin SU-8 layer loaded with Rhodamine-B, enabling high resolution surface temperature imaging via fluorescence thermometry. The heaters, however, remained only as a heat source. Solutions relying on fluorescence thermometry at the time of use (or other contactless methods) are not readily compatible with single-chip integration or point-of-care use.

The work of Selva *et al* is of particular interest. In that work, a Cr/Au heater underlying a chamber was embedded in an SU-8/PDMS structure built on silicon. The heater was optimized to compensate for edge cooling and provide uniform temperature constrained within the chamber area. The authors, however, did not utilize the heater as a sensor, and instead relied on fluorescence thermometry to measure the temperature in the chamber during operation. However, their work is an elegant demonstration of a polymeric/Si structure with a temperature uniformity of better than ± 1 C in the chamber itself. For our applications, we have found that we need an overall temperature reproducibility and chamber uniformity of about ± 1 C or less. We have also found that with our previous designs of minimalist instrumentation (i.e. aiming for portable point-of-care use), environmental variations such as irreproducibilities in thermal contact to a heat sink, changes in ambient air temperature, air flow or humidity can all lead to a lack of reproducibility.

In the present work, we sought a means of reliably attaining the above criterion (± 1 C) without having to control environmental parameters such as the heat sink temperatures and ambient air temperature or velocity. We refer to this as thermal robustness.

This work presents a manufacturable lab-on-chip implementation where a thin film Al heater is intimately integrated with a PCR chamber and is simultaneously used as a temperature sensor. Moreover, the thermal resistance from the heater to the chamber is orders of magnitude lower than the resistance from the chamber to the environment. This configuration has several distinct advantages: (1) the system becomes largely insensitive to variations in external factors; (2) the chamber and heater temperatures are essentially the same; (3) the thermally controlled regions are isolated from the silicon and can be operated independently. The system is readily controlled and need not be calibrated before use if the temperature coefficient of resistivity (TCR) of the Al film is known.

In past work we have demonstrated a range of desktop systems capable of performing complete genetic diagnostics with minimal support [14, 15] using a technology based on glass microfluidics and discrete electronics and optics. We are now in transition to a new system based on single-chip integrations of polymeric microfluidics atop CMOS electronics. To be cost-effective, such CMOS substrates need to be mm-scale, requiring that all of our procedures be moved to a platform that is significantly smaller than many lab-on-chip formats. As part of that transition, we have developed and demonstrated mm-scale length separations in microchannels for genetic analysis (e.g. [16]), integrated electrically controlled valves [17], CMOS-based HV generation [18], and CMOS-based laser-induced fluorescence detection [19]. In more recent

work, we have developed methods of integrating photopolymeric microfluidics [20] with integrated heater/sensor films [21]. In the present work, we apply these to implement robust silicon-based thermal control. All of our silicon, CMOS and photopolymer (KMPR-based) work has been developed in tandem with a CMOS and MEMS manufacturer (Teledyne-DALSA Semiconductor, TDSI) with a view to making the technologies available for manufacture as they are developed. Although we have used KMPR as a photopolymer, the advantages of the present design in terms of thermal control could be realised with a wide range of alternatives such as SU-8. KMPR was selected as the photopolymer because it is a material that is readily spin-coated and photopatterned with extremely good precision. KMPR also has extremely good adhesion to both the silicon substrate and metals.

In this work, we developed a simplified analytical model for the thermal system, verified that model and the resulting design via simulation and fabricated the designs with a CMOS-compatible process. We have also validated these predictions experimentally by means of two independent temperature measurement methods, one electrical and one optical. The agreement of all of these models and methods indicates that the system is thermally robust, i.e. can be temperature controlled within about 1 C in a manner that is largely independent of the external parameters. This, and the CMOS compatibility of the underlying fabrication technologies, indicates that it can implement the temperature control needed by a wide range of molecular biology processes and is suitable for commercial mass-manufacture without a requirement for device-level calibration. To our knowledge, this is the first manufacturable implementation of a thermally robust, CMOS-compatible lab-on-chip system suitable for PCR.

2. Design, methods and materials

To show the viability of the approach we first developed an idealised one-dimensional (1D) analytical model for the system, and used this to estimate parameters that describe how the behaviour is affected by changes in the environment. Simulations were subsequently used to validate the design, as well as to refine these parameters. Finally, we fabricated the device and tested its robustness with two temperature measurement methods, one based on the electrical parameters of the system and one based on temperature dependence of fluorescence.

2.1. An analytic model

2.1.1. Concept of the 1D model. The thermal structure consists of a thin film aluminum heater that has a $1550 \mu\text{m}$ radius, that underlies a circular PCR chamber that has a $1200 \mu\text{m}$ radius. The heater is embedded in a multilayer KMPR polymer structure built upon a Si substrate, as shown in figure 1. The thicknesses of the KMPR layers are (from bottom to top) 20, 20, 20 and $25 \mu\text{m}$. These layers support a variety of microfluidics for the implementation of molecular biology, notably microchannels and vias as well as the chamber shown in figure 1. The entire device is placed onto a heat sink. We have implemented

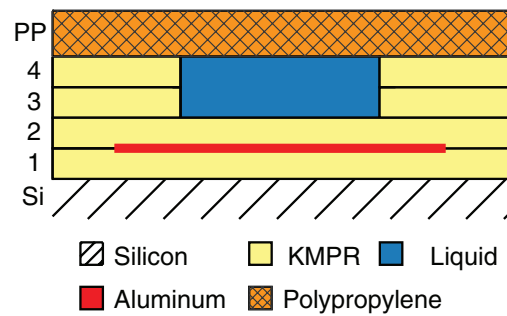


Figure 1. Cross-sectional view of photopolymer (layers 1–4) and heater layers stacked atop a silicon substrate. The device is placed onto a heat sink prior to operation. The topmost layer (PP) is either a polypropylene membrane or a tape. Corresponding thicknesses are shown in table 1.

multilayer microchannels in KMPR by patterning layer 2–4 in similar structures [20]. The uppermost polymer layer forming the roof is made of a polypropylene (PP) membrane (or, alternatively, a PCR-compatible tape). In future work, this cap might be replaced by KMPR layer 4. This roof and the underlying Si substrate are $40 \mu\text{m}$ and $500 \mu\text{m}$, respectively, while the designed thickness of the Al heater is 100 nm .

The first KMPR layer (1, using the numbering scheme of figure 1) limits the power requirement of the device by insulating the heater from the Si substrate and the heat sink below it. Layer 2 isolates the PCR sample from the heater/sensor and smooths out the large temperature ripple resulting from the structure of the heater. Layers 3 and 4 are patterned to make up the chamber, channels and fluidic ports. Finally, a polypropylene lid seals the chamber and contains the pressure generated by the heated liquid and allows for Grover-style [22] valving.

To conserve power, the heater is extended only enough beyond the chamber to ensure uniformity in the chamber. Since thermal transport is a diffusive process, we estimate that this distance should be at least twice the thickness of the polymer stack (which is $125 \mu\text{m}$ in total). In other words, we would expect that edge effects can be (at least to first order) neglected as long as the heater extends beyond the chamber by $250 \mu\text{m}$ or more. We would expect that most of the temperature change will occur within a range of about $125 \mu\text{m}$ from the outermost edge of the heater.

2.1.2. A thermally resistive divider design

2.1.2.1. Vertical thermal resistance. Rather than deal with bulk parameters such as the thermal conductivity, it is common to describe such systems in terms of their thermal resistances. As discussed in [23] and elsewhere, there is an analogy to be drawn between the voltage difference, current and electrical resistance and the temperature difference, heat flow and thermal resistance in units of K, W and $\frac{\text{K}}{\text{W}}$ respectively. With the heater suitably extended, the temperature in the chamber region is expected to be uniform, and this allows the use of a 1D approximation wherein we consider the heat to flow vertically through the various layers. Each layer of area A (in units of m^2), thickness d (in units of m) and thermal conductivity k (in units of $\frac{\text{W}}{\text{m}\cdot\text{K}}$), contributes a vertical thermal resistance

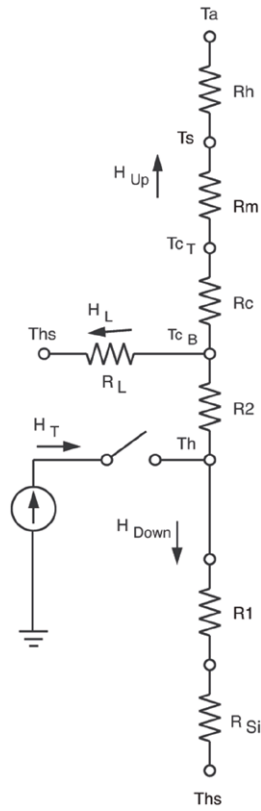


Figure 2. A thermally resistive divider where the resistances are described in section 2.1.2, with values determined for the various layers shown in figure 1 shown in table 1.

of $R_{\text{layer}} = \frac{d}{kA}$. The heat flow across any layer (H , in W) is a linear phenomenon with $H = \frac{\Delta T}{R}$, where ΔT is the temperature difference and R the thermal resistance.

In the system depicted in figure 2, where each of the layers gives rise to a thermal resistance, the heat flow will produce well-defined temperatures at each of the nodes. As a result, we can estimate the temperatures at any point in the resistive divider structure and use this to estimate the robustness of the system against variations in external parameters such as the heat sink temperature (T_{hs}) and the ambient temperature (T_a).

The resulting layer resistances are: R_m for the membrane, R_c for the water-filled chamber, R_1 for KMPR layer 1, (and similarly for KMPR layers 2–4), R_{Si} for the Si substrate and these are tabulated in table 1. The various temperatures are: T_s for the chip top surface, T_{ct} for the chamber top surface, T_{cb} for the chamber bottom surface, and T_h for the heater. The thermal conductivity for KMPR has not been reported, so that of SU-8 is used, as this is a similar epoxy-based photopolymer [24, 25] and is well-characterised. (The temperatures will be found to be relatively insensitive to variations in this thermal conductivity.)

2.1.2.2. Lateral thermal resistance. The lateral resistance, R_L , caused by edge effects can be approximated by considering the thermal resistance of the cylindrical section [23] formed by the region of the polymer stack between the edge of the chamber and the edge of the heater, following: $R_L = \frac{1}{2\pi kd} \ln\left(\frac{r_2}{r_1}\right)$,

Table 1. Thermal conductivities and resistances for a 1550 μm radius heater operating at 95 C.

Material layer	Conductivity $k\left(\frac{\text{W}}{\text{m} \cdot \text{K}}\right)$	Thickness (μm)	Resistance $\left(\frac{\text{K}}{\text{W}}\right)$
KMPR 1,2,3 ($R_{1,2,3}$)	0.2	20	13.9
KMPR 4 (R_4)	0.2	25	16.5
PP membrane (R_m)	0.22	40	26.5
Water (R_c)	0.67	45	8.9
Si substrate (R_{Si})	163	500	0.40
Al heater	237	0.1	≈ 0
Convection (R_h)			23 628
Lateral (R_L)			387

Note: Layers are labeled as in figure 1.

where r_1 is the inner radius; r_2 is the outer radius; k is the thermal conductivity; and d is the thickness of the cylinder, which may simply be taken as the total thickness of the structure. As discussed in section 2.1.1, we expect any edge effects to occur in the 125 μm outside the heater edge. For the purposes of estimating the lateral resistance then, we take $r_1 = 1550 \mu\text{m}$ and $r_2 = r_1 + 125 \mu\text{m}$.

Clearly, a very thin, low-conductivity structure can dramatically increase the lateral resistance and reduce the horizontal heat loss. If this loss is made negligible, the heat will be constrained to flow vertically, turning the device into a 1D system where the chamber temperature can be determined from the heater temperature through a simple analytical relationship, with small adjustments for external parameters such as the ambient and heat sink temperatures. These parameters can be refined by three-dimensional (3D) simulation. If the polymer layers are thin enough then the device will be insensitive (i.e. robust) to these external parameters (e.g. variable airflow or room air temperature).

2.1.2.3. Convective losses. Heat loss at the top surface is taken to occur by natural convection with a heat transfer coefficient (h_{tc}) [26] of $5.6 \frac{\text{W}}{\text{m}^2 \cdot \text{K}}$ and resulting in an effective thermal resistance of R_h where: $R_h = \frac{1}{h_{\text{tc}} \cdot A}$.

2.1.2.4. Chamber size and power needs. Given the chamber and heater sizes of section 2.1.1, the power required for operation can readily be estimated from the thermal resistances, giving $H_T \approx \frac{T_h - T_{\text{hs}}}{R_1 + R_{\text{Si}}}$ or about 5 W for the present 1550 μm design. These powers are readily tuned for any given application. Once the uniformity is well-characterised, we expect to miniaturise these devices further (along with their required powers). Since these powers scale inversely with the square of the radius, the overall power can readily be brought well below 1 W.

2.1.3. Robustness. To show the robustness of this simplified analytical model with a temperature controller keeping the heater at a constant temperature, we consider the effects of lateral conduction and convection separately. Fluctuations in the temperature of the ambient and the heat sink will induce changes in the chamber temperature even if the heater

temperature is held constant. The magnitude of these fluctuation can be estimated from the thermal resistances given above. We consider the situation with the heater held at 50 C with a T_a and T_{hs} of 25 C. We chose 50 C as it is representative of the annealing temperatures of the PCR process—the most sensitive stage of PCR.

2.1.3.1. Robustness against convective variations. The reported values of h_{tc} for free convection on heated surfaces may differ by a factor of four [27] or more, depending on conditons. For the convective component, considering heat flow through R_2, R_c, R_m and R_h , we would estimate the temperature difference between the heater (T_h) and the chamber bottom, T_{cb} , as:

$$T_h - T_{cb} = \frac{R_2}{R_2 + R_c + R_m + R_h}(T_h - T_a) \approx \frac{13.9}{23\,628}(25) \approx 0.015\text{ C}$$

and we define the term γ such that:

$$T_h - T_{cb} = \gamma(T_h - T_a)$$

so $\gamma \approx \frac{0.015}{25} \approx 0.0005$ (no units). The term γ is the amount of change in the chamber temperature that will be introduced if the air temperature is changed by a degree K while the heater temperature is held constant.

This estimate of γ is based on a simple approximation and is intended to provide only an estimate of the overall sensitivity to changes in ambient temperature and air flow. However, it is clear that the loss by conduction is dominant to the extent that even a large change in the h_{tc} value (e.g. a factor of 4) or temperature (e.g. 10 K) does not affect the result significantly (i.e. the resulting change in chamber temperature is $\ll 1$ C. Hence, although we expect the convection and room temperature to vary, their effects are expected to be negligible and this design is therefore robust against convective variations. If a temperature controller were used to hold the heater temperature constant, then the chamber temperature would be insensitive to external variations due to convection—i.e. this is a thermally robust design in terms of convection.

2.1.3.2. Robustness against conductive variations. For the lateral conduction, considering heat flow through R_2 and R_L from the heater through the periphery (through R_L) and to the heat sink (through R_2), we would estimate the temperature at the chamber bottom (at the wall), T_{cb} , as:

$$T_h - T_{cb} = \frac{R_2}{R_2 + R_L}(T_h - T_{hs}) \approx \frac{13.9}{387}(25) \approx 0.90\text{ C}$$

and we define the term β such that:

$$T_h - T_{cb} = \beta(T_h - T_{hs})$$

so $\beta \approx \frac{0.9}{25} \approx 0.04$ (no units). The term β is the amount of change in the average chamber temperature that will be introduced if the heat sink temperature is changed by a degree K while the heater temperature is held constant. This parameter is small but significant. As an example of its effect: If a temperature controller is used to keep the heater temperature constant, a change in heat sink temperature by 10 K is expected to lead to a change in the chamber temperature of about 0.4 K. To

summarise, although the heat sink temperature will vary, to first order the resulting changes will only affect the chamber temperature via vertical conduction and this will be uniform and (as will be seen below) easily dealt with via a controller. If such a temperature controller were to be used to hold the heater temperature constant, then the chamber temperature would be insensitive to external variations due to conduction—i.e. this is also a thermally robust design in terms of conduction.

2.2. Determination of temperature from TCR

We can estimate T_h directly from the heater resistance following: $T_h = T_0 + \frac{R_{eh} - R_{eh0}}{\alpha R_{eh0}}$ where α is the TCR in units of $\frac{1}{K}$, T_0 is the room temperature, R_{eh0} is the room temperature electrical resistance of the heater, and R_{eh} is the actual operating electrical resistance of the heater. As shown in the previous section $T_c \approx T_h$. However, since the edges of the heater are cooler when it is actively heating, (as opposed to when it is being characterised in an oven), a more accurate expression would be:

$$T_h = T_0 + \frac{R_{eh} - R_{eh0}}{\epsilon \alpha R_{eh0}} \quad (1)$$

where ϵ accounts for the fact that a small portion of the heater is not at a uniform temperature. Since this cooler region is small, we expect ϵ to be slightly smaller than 1. We refer to the $\epsilon \alpha$ as being the effective TCR whereas the TCR itself (i.e. α) is determined separately by direct measurement.

Although a more accurate estimate will be made from simulations in section 2.8.1, it is instructive to estimate the value of ϵ from first principles. Much as described in section 2.1.2, if over the transition zone from 1550 μm to 1550 + 125 μm the temperature varies from the uniform internal value to room temperature, then we could approximate this situation as being one with a uniform temperature from the centre to 1550 + 62.5 μm and an unheated zone further out. In other words, it is as if the outermost region is not heated. Since the resistance varies linearly with the temperature, we would expect the effective TCR would be scaled by the ratio of the heated and unheated areas, i.e.:

$$\epsilon \approx \frac{\pi(1550 + 62.5\mu\text{m})^2}{\pi(1550 + 125\mu\text{m})^2} \approx 0.92$$

2.3. Offset of chamber and heater temperatures

In summary, using a simple analytical resistive divider model, a preliminary estimate of the impact of the thermal convection and conduction paths indicates that this design will require the use of correction factors to obtain the chamber temperature from the heater temperature. Fortunately, these factors are small. As a result, we can estimate the chamber temperature as:

$$T_c = T_h + \beta(T_{hs} - T_h) + \gamma(T_a - T_h) \quad (2)$$

where T_h is given by equation (1).

The parameters α , β , γ and ϵ will be better determined below, with α derived from measurement and the others via

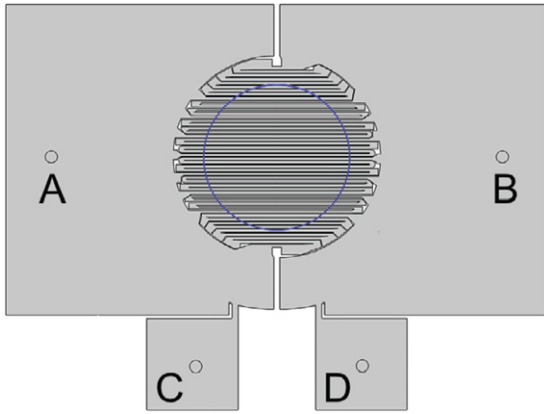


Figure 3. Layout of the heater. The circle indicates the perimeter of the 1200 μm radius chamber. The driving current is applied through terminals (A) and (B); the output voltage is probed between terminals (C) and (D). The circles indicate points of electrical contact.

simulations in section 2.8.1. Since β and γ introduce small corrections, while α and ϵ are determined reproducibly from the fabrication procedure (α), or the design (ϵ), it is clear that we have a well-defined temperature that is insensitive to unintended variation, i.e. we expect robust thermal control.

2.4. Designs and layout of the silicon chip

Each photopolymer/silicon chip was composed of a KMPR and Al layer stack atop a Si substrate (as per figure 1) and contained a set of microchannels and vias in addition to the PCR chamber itself. We designed our devices for temperature uniformity at the denaturation temperature of PCR (typically about 95 C) through a series of two-dimensional (2D) axisymmetric simulations that gradually extended the heater beyond the chamber until a chamber uniformity of ± 0.5 C was achieved. COMSOL Multiphysics version 4.3, with the MUMPS (MULTifrontal Massively Parallel sparse direct Solver) direct solver was used for the 2D and 3D simulations of the present work. The temperatures for the heat sink and ambient were $T_{\text{hs}} = 30$ C and $T_{\text{a}} = 22$ C. We performed simulations of uniform power density designs (with $T_{\text{c}} \approx T_{\text{h}} \approx 95$ C). All external boundary conditions were set as convective to the ambient.

A representative design is shown in figure 3. The heater was designed to provide a maximum (at 95 C) uniform power density, Q , of:

$$Q \approx \frac{k_{\text{KMPR}}}{d}(T_{\text{h}} - T_{\text{hs}}) \approx 6.3 \times 10^5 \frac{\text{W}}{\text{m}^2},$$

where d is the thickness of the KMPR layer beneath the heater.

Earlier designs of our heaters failed frequently, apparently due to electromigration at the contacts or the heater traces themselves. In revised designs, we ensured that the current density did not exceed what we set as a conservative limit to avoid electromigration, $2 \frac{\text{mA}}{(\mu\text{m})^2}$ for operation near 100 C. We note that Weste and Harris [28] suggested an electromigration threshold of $\approx 2 \frac{\text{mA}}{(\mu\text{m})^2}$ at 110 C. The present design of devices is stable and we have not detected any variations over time

frames of days of operation (more than enough time for a PCR analysis).

The trace widths for this design range from about 37–53 μm , where the width is constant across the length of the traces (shorter traces need to be narrower to have the same heat generation as the longer traces). Although there are necessarily small unheated regions between the traces, these are small enough that the thickness of the KMPR layer (with its thermally conductive layers above and below) is sufficient to adequately suppress any temperature variation. The heater is operated simultaneously as a 4-point sensor, wherein the drive current is applied through terminals A and B, and voltage is probed across terminals C and D. To reduce the total current requirement of the system, the tracks are connected in series, in groups of 3–9, and all the groups are connected in parallel to a common power bus.

2.5. Design of the chip packaging

2.5.1. Original design with integrated microfluidics. Our original intent was to use these structures in a microscale PCR demonstration with integrated microchannels and vias. An alignment jig was fabricated from PMMA and used to provide fluidic access ports and pneumatic control of the membrane (labelled PP in figure 1) atop the PCR chamber, in addition to a Grover-style valving of the microchannels [22].

Because the packaging needed to align to sub-mm features upon a mm-scale silicon chip, precise alignment was essential, especially since it is very difficult to see the smaller Si-based features through the thicker PMMA packaging. As a result, we designed the silicon chip to be diced within ± 50 μm and the packaging to provide alignment of that diced substrate to fluidic ports and vias with the same uncertainty. (To obtain this level of accuracy, all the packaging was constructed using rapid prototyping micromachining techniques with a CO_2 laser system (ULS 2.3, Universal Lasers) or CNC (MicroMill DSL3000, MicroProto/Taig). The intent was to assemble the silicon chip into the package in such a way that the overall system could be re-used many times with computer controlled loading, thermal cycling, analysis, cleaning and fluorescence detection steps much as in [15]. The assessment of the spatial uniformity of the temperature was performed using fluorescence detection via a modified microscope (as described in section 2.10).

2.5.2. Revised design without integrated microfluidics. As an alternative approach, a preliminary exploration was made with a simplified system, one in which a PCR compatible tape was used to cap the chamber after manually loading reagents with a micropipetter. As described below, this also had the consequence that the membrane that was used to seal the PCR chamber could no longer be pressurised during operation.

2.6. TCR measurements

Initial electrical tests were unreliable due to time varying resistances that seemed to be due to electromigration, especially near the contacts. As a result the electrical

measurements were made in two different ways to allow us to identify where resistances may be changing (if needed). The standard 4-point method eliminates the uncertainties in the measurement caused by resistances in series with the load, such as the contact resistance of the pins. However, since we had found the contact resistance could change with time and/or external stress such as heat and humidity, we took another approach that also allowed us to monitor contact resistances.

2.6.1. Four point measurements of TCR. The devices were placed on an aluminum heat sink ($72.5 \times 40 \times 6.5$ mm) atop a hotplate (Torrey Pines Scientific EchoTherm™ HS40). Spring-loaded Au-coated pogo pins of 1 mm diameter (Interconnect Devices Inc.) were used to contact the heater without scratching the Al film. A very thin film of thermal paste (T630 THERM-A-GAP Dispensed Thermal Gel, Parker Chomerics) was applied at the chip-heat sink and heat sink-hotplate interfaces to ensure good thermal contact. The hotplate heated the entire aluminum plate and chip and its temperature control was accurate to within 1 C. The resistance was measured with a multimeter (HP-34401A, Hewlett Packard) in 4-point mode at 22, 40, 60, 80 and 100 C (on both a ramp-up and ramp-down) and again at 22 C to verify film stability. A pause of 20 min at each temperature was allowed for the hotplate to stabilize before taking a reading.

2.6.2. Non-four point measurement of TCR. The TCR of the deposited Al layer was also measured on a chip from the same fabrication batch but in a non-standard way. The resistance between each possible pair of contact pads was measured at each of several set temperatures while the assembly was kept in a convection oven. By solving the resulting system of equations, the heater resistance *and* the contact resistances could be determined reproducibly. The heater chip was placed in a closed metal box (to minimise thermal variation due to air flow) on the rack of a forced air oven (model #6916, Fisher Scientific). A thermometer was used to measure the temperature inside the box to within ± 0.5 C. The 4 wires were attached to the chip using a low-melting-point solder (Roto144F from RotoMetal Inc.). The DMM (U1252A, Agilent) measurement repeatability was 0.01Ω . From the variation of the heater resistance versus oven temperature the TCR was obtained.

2.7. Heater control and temperature

2.7.1. Heater control. The heater was driven by a custom-designed linear voltage-to-current convertor that was in turn driven by a USB-based data acquisition device (U6, Labjack). A python script controlled the U6, gradually increasing the current to a preset level and holding it there for 200 s before stepping down. This was done for each current value. (The equilibration time was measured to be approximately 40 s). Current and voltage data were collected for each run and, for a given voltage setting, the resistance could be determined to within 0.004Ω . Using equations (2) and (1) the resistances can be used to derive T_h .

2.7.2. Calibration of temperature-dependent fluorescence. Following the method of Ross *et al* [29] we used the temperature-dependent fluorescence of Rhodamine B to non-invasively measure the chamber temperature. However, since this fluorescence is protocol dependent we first needed to calibrate the method. To determine the Rhodamine B calibration curve, Rhodamine B powder (part # 83689, laser grade, Sigma Aldrich) was first diluted in MilliQ water to 1 mM concentration and stored in a 10 mL conical tube covered in Al foil. Before use, aliquots of the 1 mM stock and $5 \times$ TBE buffer were diluted with MilliQ water to make a 100 and $10 \mu\text{M}$ working concentrations of the fluorophore. An optical spectrometer (USB4000 or a USB2000, Ocean Optics) was used (in a low-power setting), with a cuvette holder inside a styrofoam box and a thermometer in good thermal contact (using thermal paste, Part #10004, Cortec Spray Technology) and a LS-450 light source with a 518 nm LED. The cuvette holder was heated by a circulating water bath (Model S-1, MGW Lauda). A cuvette filled with 1 ml of the solution was placed in the holder. In order to fully equilibrate the system, the water temperature was increased in 2 C steps from 30 C to 78 C and held at the set temperature for half an hour before taking each measurement. The LED excitation illumination was only turned on when needed, and this, along with the use of low illumination powers, avoided photobleaching effects. After initial testing with the $100 \mu\text{M}$, further work used the $10 \mu\text{M}$ concentration. At each temperature, the intensity was averaged over the range 580–585 nm, and over 10 spectra. (The peak wavelength for this Rhodamine B in $1 \times$ TBE was 583 nm) This value then normalised to the value obtained at 22 C. The data were then fitted using the polyfit command of the MATLAB package (MATLAB, MathWorks, MA, USA).

2.7.3. Determination of chamber temperature from temperature-dependent fluorescence. An image of the chamber showed a level of fluorescence that varied with the temperature, following the calibration curve described in section 2.7.2. Although CCD cameras are often used in low-light conditions, we found that their integration times were incompatible with our rapidly changing signals. As a result, we used a high resolution CMOS and this generated rather small signals (e.g. 25 counts per pixel) with significant levels of noise (several counts). However, with the large numbers of pixels in the camera, signal averaging allowed the noise to be easily handled in the central, brightly illuminated regions of the chamber. However, the signal became difficult to detect near the edges of the chamber through a combination of relatively poor illumination and reflections from the chamber edges. As a result, when determining the chamber temperature, the pixel values were averaged (using a tool within ImageJ) over a 600 pixel diameter (corresponding to $900 \mu\text{m}$) around the chamber centre.

2.7.4. Determination of temperature uniformity from fluorescence. The temperature uniformity was analysed with a 2D method by comparing the images of the fluorescence at the elevated temperature and at room temperature. Much as previously described, an image of the chamber at an elevated

temperature is subtracted from an image of the chamber after multiplication by a scaling factor. This scaling factor is chosen to bring the resulting image signal to zero in the region of interest. Because of the need to deal with the edge effects (as above) and the noise within the signals, aggressive signal averaging was needed. This procedure was implemented by reading the images into Python numpy arrays for the scaling and using a Gaussian to average over the nearest 50 pixels. Even so, reflection effects and the absence of signal in the non-illuminated region required that the region outside the central 600 pixel diameter (900 μm) portion of the chamber be masked off. The final array can then be displayed as a contour plot using matplotlib. The variation of the number of counts can be related to the variation of the temperature using the calibration curve. (Given the large amount of noise in the raw data we have sought to use a method that is as linear as possible, thereby avoiding the direct use of the temperature calibration).

Once a region without any anomalies has been found (i.e. a well-illuminated region with no reflections), the temperature uniformity can also be assessed with a 1D method by performing running averages along a path in each of the two images. The ratio of the resulting running averages can then be used with the calibration curve to extract the temperature along the path.

2.8. 3D simulations to verify behaviour

2.8.1. Sensitivity factors from 3D simulations. The sensitivity of the system to variations in T_{hs} and T_{a} was assessed by simulation on the full 3D model of the system by embedding the actual chip design shown in figure 3 in a fully coupled Joule-heating/heat-transfer 3D FEM model. The simulation tool calculated the heater resistivity pointwise as a function of temperature using the values of $3.52 \times 10^{-3} \text{ K}^{-1}$ for the TCR and an electrical resistivity of $\rho = 4.39 \times 10^{-8} \Omega \cdot \text{m}$. These are the values we had reported earlier for Al films on KMPR [21]. Since the information being sought was that of the sensitivity factors, the simulation was insensitive to the actual values used for the resistivity and TCR. This is fortunate since these parameters will vary considerably depending on deposition conditions (notably thickness and base pressure).

In the simulation, the applied voltage, V_{app} , across terminals A and B in figure 3 was specified and the current through the heater, I , was determined. The heat sink temperature is specified while the other boundaries have a convective heat loss boundary condition. In order to quantify the sensitivity to T_{hs} the system was first simulated with $T_{\text{hs}} = 20 \text{ C}$, with values of V_{app} from 1.5 to 12 V, in steps of 1.5 V. The T_{a} was fixed at 20 C. The average chamber temperature T_{c} and the heater resistance R_{h} were recorded at each simulated point. The value for T_{c} was calculated as the volume integral of the temperatures in the chamber divided by the total chamber volume. The resistance was calculated from the output voltage between C and D, V_{oc} , divided by the total current, I . The simulation was repeated for $T_{\text{hs}} = 30 \text{ C}$ and 40 C . Lines of T_{c} versus R_{h} were then fitted through the data obtained for each of the three values of T_{hs} . If a controller held the heater temperature constant (and hence

its resistance) the spacing between the three lines would represent the change in T_{c} brought about by the variation in the T_{hs} . By dividing the vertical distance (in T_{c}) between the fitted lines by the change in T_{hs} we can obtain a value for β . The T_{a} data can be treated similarly to provide a value for γ . Finally, a comparison of the simulated resistance R versus the known temperature in the uniform region provides a measure for the proportion of the chamber that is heated, i.e. ϵ .

2.8.2. Temperature uniformity from 3D simulations. The simulations (as described above) allow us to accurately assess the temperatures within the chamber. The resulting data from any one of the simulations can be plotted, most informatively as a top view of the chamber bottom. Similarly, the data can be analysed to provide minimum and maximum temperature estimates in the chamber region.

2.9. Fabrication of the photopolymer/silicon chip

Devices were fabricated using academic facilities at the U. of Alberta, where we have been developing experimental fabrication procedures using a photopatterned polymer (KMPR). These procedures have been tailored to research objectives such as the development of Al heaters [21] on KMPR and multilayer microfluidics with KMPR [20]. These processes mirror a commercially available technology offered by TDSI. Although the commercial process is well-developed, the academic process is readily adapted to accommodate experimental fabrication procedures.

For the present work, our devices used photopatterned KMPR (KMPR 1025, Microchem Corp.), upon either silicon or 4 inch square Borofloat substrates, which was then thermocompressively bonded. Our procedures were much as previously described [21]. In brief: the test grade 4 Si substrates were cleaned and prepared for use by immersion in a freshly prepared Piranha solution (3:1 $\text{H}_2\text{SO}_4:\text{H}_2\text{O}_2$) for 15 min prior to being rinsed with deionized water, dried using N_2 and dehydrated on a hotplate at 150 C for 15 min. Successive KMPR layers were spin-coated onto the substrates and photopatterned. We had previously reported on the patterning of Al heaters on KMPR by standard lithography. The power density profile produced by the heater is highly dependent on the width of the metal tracks, to the extent that a lift-off technique was used to avoid undercut and respect the designed shape of the tracks. A 50 nm thin Cr film was sputtered (300 W, magnetron sputtering) onto the crosslinked KMPR using an Ar deposition pressure of 8.5 mTorr to reduce film stress. This film served to protect the KMPR during the lift-off process for which we used HPR 504 as a positive lift-off photoresist. A 1.25 μm thick film of the resist was patterned on top of the Cr film to form the heater shapes. Following development, the newly exposed Cr was etched away to allow the heater to be deposited directly onto the KMPR. Once etching was completed, an Al film was deposited by sputtering (300 W, 7 mTorr Ar), for a nominal 100 nm thickness. Lift-off was performed by sonicating the substrates in acetone to remove the remaining HPR 504 resist (and the Al deposited on top of the resist). Lift-off typically required between 5 and 10 min to

fully remove the excess Al. Once lift-off was complete (and verified using an optical microscope), the remaining Cr on the substrate was stripped off to leave only the heater remaining on top of the KMPR film. Successive layers were assembled through a combination of bonding and photolithography of newly spun material. The bonding of photopolymer layers used a hot embosser (Jenoptik HEX02) and allowed for the formation of devices with a fully enclosed microfluidic network with channels, vias, access ports, valves and a micro-volume PCR chamber of 1200 μm radius and 45 μm depth. These devices, much as shown in figure 1, were then diced in a dicing saw (Disco DAD321).

2.10. Fluorescence-based determination of chamber temperature

A proprietary absorbing color filter (much like a long-pass filter with a wavelength cut-off at ≈ 560 nm) was obtained from TDSI. A Kingbright LED with a centre wavelength of 465 nm (Part# WP710A10QCB/G, Digikay) was used as an excitation light source. A microscope (Micromaster, Fisher) was modified to place the filter on top of the objective lens. The original eyepiece was replaced by a CMOS camera (model # MU900, Amscope) with a C-mount relay lens adapter to capture the real-time image of the chamber fluorescence.

The Kingbright LED was angled at about 60 degrees for better illumination and attached to a PMMA plate that provided alignment above the PCR chamber. The Amscope camera was operated using its software (Toupview) to acquire a steady stream (1 image every 2 s) of jpeg images under fixed conditions of exposure time and contrast. These images were saved directly to computer disk. The PCR chamber was filled with the Rhodamine solution and imaged under a microscope. For synchronization, the image acquisition and heater current program were turned on at the same time. The collected images were processed in ImageJ [30].

Since the power (of Joule heating) is approximately proportional to I^2 and the temperature change is approximately proportional to the power, the currents required for any given steady-state temperature could readily be estimated. The current was ramped up in 20 equal steps of 2 s duration, until reaching the current for the target temperature, and then held for 200 s. Electrical and optical signals were recorded both during the ramp up and the holding period. This procedure was repeated for various temperatures with the system being left for a period of inactivity of 20 min between runs to allow for cooling. To correct for photobleaching effects, the fluorescence of the 100 μM solution was measured at room temperature before and after the above measurements were made.

3. Results

3.1. The optical calibrations of fluorescence

Using the method described in section 2.7.2, the calibration curve of figure 4 was obtained. The calibration runs were performed on two successive days with the same sample. A

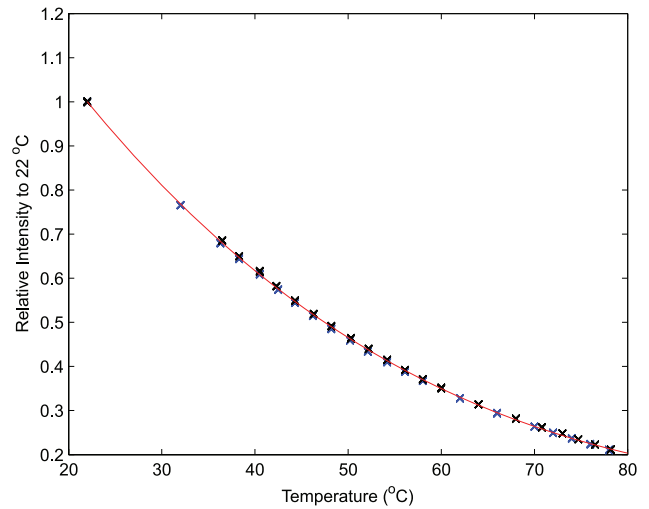


Figure 4. Temperature-dependent fluorescence calibration curve of 10 μM Rhodamine B in 1x TBE from two successive calibration runs, as described in section 2.7.2.

third set of measurements was done using a qPCR machine (CFX96, BioRad) by using a melt curve analysis program and the HEX filter set of the instrument. All three sets of data were consistent.

A cubic function was used to fit the data shown in the RhB calibration curve of figure 4, resulting in the calibration equation of equation (3), where F is the fluorescence light intensity normalized to the value at 22 C and T_c is the chamber temperature. The uncertainty in the resulting T_c is estimated to be ± 0.35 C.

$$T_c = 118.4245 - 239.506F + 245.15F^2 - 102.19F^3 \quad (3)$$

3.2. Fabrication results

3.2.1. Fabrication of the photopolymer/silicon chip and its packaging

3.2.1.1. Results of fabrication of chips with integrated microfluidics: An example of the U1550 devices is shown in figure 5, where the lighter-coloured square regions are the electrical contact points (i.e. no KMPR) and the microchannels terminate in access wells. The Al thickness measured in the fabricated devices was $h = 150 \pm 10$ nm and this produced a typical heater resistance of 20 Ω . Using the 4-pt method, two devices of the same fabrication batch calibrated on a hot-plate showed a TCR of $2.07 \pm 0.019 \times 10^{-3} \text{ K}^{-1}$. The result obtained from using the second, non-4 point, method to obtain the TCR was in good agreement. This oven-based TCR was $2.06 \pm 0.05 \times 10^{-3} \text{ K}^{-1}$. Although these values are consistent, they are quite different from those obtained in previous work [21]. In that previous work we measured a TCR of about 1.5 times higher, in a film that was also about 1.5 times thicker. This difference is not surprising since TCRs are known to vary strongly with thickness.

The packaging had been intended to make a snug fit with the fabricated chip in order to provide pneumatics, fluorescence detection, fluidic interface, electrical interface and thermal control. However, substantial yield issues arose in

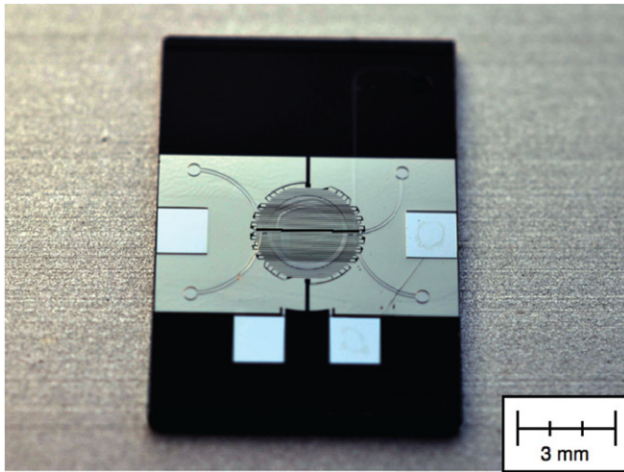


Figure 5. Top view of a fabricated multilayer KMPR/Si device. The largely transparent polymeric multilayer structure is as shown in figure 1 with the design shown in figure 3 without the topmost layer and with microchannels accessing the chamber.

the fabrication of the photopolymer/silicon chips, notably in terms of the dicing and the definition of the microchannels. Substantial play in the dicing machine led to the majority of the diced silicon chips not being able to fit into the micromachined packaging. Similarly, it appears that the optimisation of the photopolymer process for metallization and multilayer bonding seems to have degraded the patterning of the microchannels with the result that the microchannels were frequently not open throughout their length. We had a limited number of the photopolymer/silicon chips and we were unable to identify any functional devices that met the necessary specifications for use with the pre-built packaging.

3.2.1.2. Results from revised design without integrated microfluidics. Instead of using the complete pre-built packaging, we rebuilt part of it with looser tolerances to provide electrical interface and thermal control while allowing optical inspection via the modified microscope. In the place of the polypropylene membrane we then used a remarkably strong adhesive tape that is designed for use with PCR (AB-1170, Fisher Scientific). This tape can reliably seal without pneumatics. However, the absence of on-chip valves required that the chip be disassembled and cleaned after each use (rather than being reusable as originally intended) and this disassembly often led to the destruction of the chip.

3.2.2. The determination of the sensitivity factors via 3D simulation. The series of 3D simulations gave rise to fitted lines that were offset by ≈ 0.486 K by a 10 K change in T_{hs} (thereby giving a $\beta \approx 0.0486$). Similarly, they were offset by ≈ 0.0436 K by a 10 K change in T_a (thereby giving a $\gamma \approx 0.00436$). These parameters and that of ϵ are shown in table 2. There is an agreement in terms of general magnitude between these—although we cannot expect a close agreement given the approximate nature of the initial 1D estimate. These results confirm, from 3D simulation, that the system is robust to variations of T_{hs} and T_a .

Table 2. Sensitivity factors determined from initial estimates and from 3D simulation.

Source	β (unitless)	γ (unitless)	ϵ (unitless)
1D estimate	0.04	0.0005	0.92
3D simulation	0.049 ± 0.003	0.0044 ± 0.002	0.963 ± 0.001

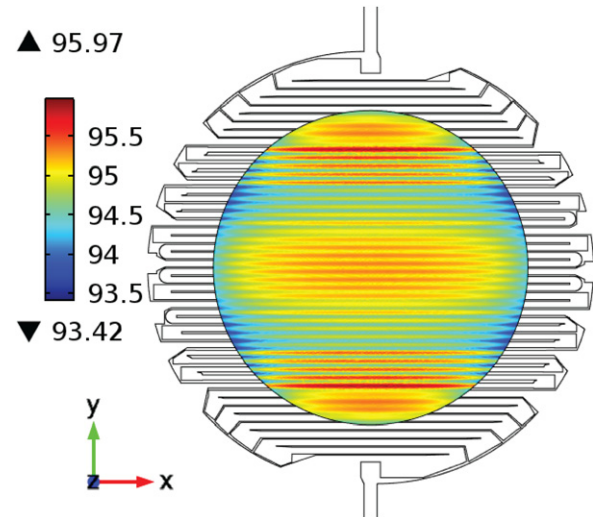


Figure 6. Top view of chamber temperature distribution from 3D simulations of the U1550 design with 10.62 V applied, giving an average chamber temperature of 95 C and a variation of ± 1.25 C.

3.3. The determination of uniformity and temperature accuracy via 3D simulation

Reaching an average chamber temperature at 95 C in the 3D models required the application of 10.62 V (with $T_{hs} = 30$ C, $T_a = 22$ C) and, as shown in figure 6, produced predicted temperature uniformity of ± 1.25 C. Clearly, the uniformity at lower chamber temperatures would be proportionally better still.

3.4. Determination of temperature from optical and electrical measurement

Fluorescence and electrical measurements were made at temperatures up to approximately 70 C, although above 50 C sufficient numbers of bubbles formed that the validity of the fluorescence-based temperature measurements became questionable. Successive runs at temperatures less than 45 C showed excellent agreement between the optical and electrical temperature measurements (as derived from figure 4 and from the electrical resistance respectively). The temperatures could be calculated from the observed electrical resistance and the parameters of table 2 and equation (2), or from the observed fluorescence using the formula of equation (3).

3.4.1. Determination of temperature uniformity from temperature-dependent fluorescence. Using the 2D method of section 2.7.4 on elevated and room temperature images found a scaling factor of 0.535 nulled the signal in the near central region. A region of zero counts therefore has a temperature of 45.2 ± 0.4 C. Figure 7 shows these results, indicating

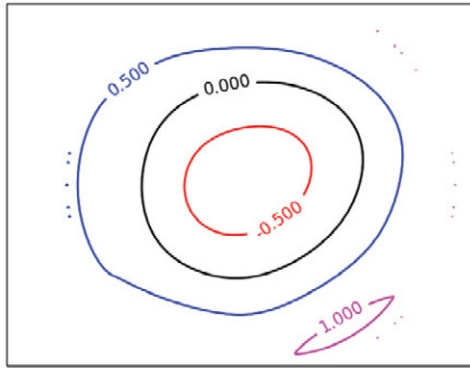


Figure 7. Result of subtracting the image of chamber fluorescence at an elevated temperature from the scaled (by a factor of 0.535) room temperature image, as described in section 3.4.1, showing a typical variation of ± 0.5 counts, corresponding to approximately ± 1 C. The exception to this is the region at the bottom right near where a bubble has apparently raised the nearby temperatures. The region shown is the central $\approx 900 \mu\text{m}$ of the $1200 \mu\text{m}$ diameter chamber.

a reasonably flat, relatively uniform field with a slightly cooler (i.e. more fluorescence in the heated image, hence cooler) central region. The cooler central region may be due to the high thermal mass of the water in the chamber, which delayed the heating of the chamber during this heating phase. The contour line for a signal level of 1.0 appears to be due to a bubble that was readily apparent in the original images (data not shown). Although this bubble was in the masked off region, the averaging process allowed it to affect the analysed region. In contrast with the bubbles seen at elevated temperatures, this bubble was present from the initial loading of the chip and did not change in size during processing.

Using the 1D method of section 2.7.4, a running average over 200 pixels ($300 \mu\text{m}$) through the centre of the chamber (corresponding to left to right through the centre of figure 7) we were able to extract a radial temperature profile that was constant to within 0.65 C.

3.5. Temperature robustness from optical and electrical measurement

The average temperature, as determined by the fluorescence measurements, and the electrically-derived temperatures were in good agreement at these lower temperatures. As shown in figure 8, the two measures tracked each other as the heater current was increased. Although the current was held steady at this point, the heat sink was slowly warming up during the run and was found to be slightly warm to the touch after the experiment. This ongoing warming of the heat sink led to the continuing increase in the chamber temperature even though the current was held steady, corresponding to an increase in the heat sink temperature of about 3 C during the run shown in figure 8. If we had used a temperature controller, it would have decreased the applied current to keep the resistance (and hence temperature) constant. Although the heat sink was warming up, and both the electrically-derived and the fluorescence-derived temperatures increased over time, they remained in good agreement. Since the electrically-derived

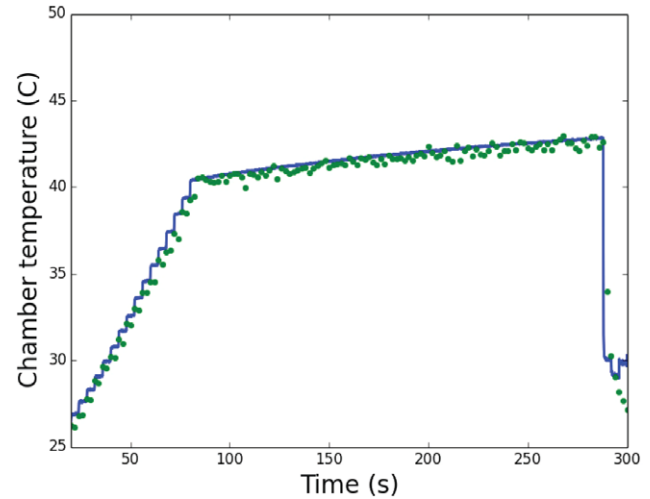


Figure 8. Optically (green dots, see section 3.4.1) and electrically (solid blue line, see section 2.2) derived temperatures compared over a heating ramp and hold period. For the ramp phase, $t \lesssim 80$ s, the control program increased the input current in steps to reach 250 mA, while during the hold phase, for $80 \text{ s} < t < 280 \text{ s}$, the heater input current was held at 250 mA as programmed. The slope of the lines in the latter period are attributed to the heat sink warming up by several C. For $t > 280 \text{ s}$, the divergence between the two traces is because the heater current has been reduced to a level that is too low to make reliable measurements. The steady agreement for the central part of the run indicates that even as the most important external parameters change significantly, the two temperatures track each other within 0.3 C.

temperature is in agreement with the optically-derived one, the electrically derived temperature could be used with a temperature controller to maintain a constant temperature, even with external variations. This was therefore a successful demonstration of robustness.

Although runs were made at higher temperatures (from 45–70 C), bubbles appeared in the chamber and these significantly distorted the fluorescence intensities by creating spatially varying concentrations of dye, as well as by giving rise to spatially varying temperatures (due to an insulating air layer). In the past we have been able to suppress the bubbles at temperatures as high as 95 C by applying a pressure of 20 psi to the membrane atop the chamber. Unfortunately, it was not possible to suppress these bubbles without the ability to apply high pressures. The electrical measurements were found to track the optical measurements until the nucleation and growth of bubbles at higher temperatures. This was verified by tracking the optical and electrical temperatures as images were taken during the heating of the chamber. (data not shown) Several runs of the chip were made as described above (i.e. from 40 to 70 C) during which bubbles always formed at temperatures higher than 45 C.

Whether due to localised heating associated with the bubbles or a degradation of the heater due to the combined action of elevated temperature and humidity, during the eighth run, the chip failed due to a localised nonconductive region that appeared beneath one of the bubbles. We note that there was some indication that these photopolymer devices were more vulnerable to water at elevated temperatures than in our past

work [20] and this is under investigation. We have since found that photopolymer layers from TDSI do not show this water sensitivity.

4. Discussion

We have validated our designs and devices by showing a good agreement between models, simulations and an experimental measurement of temperature via two independent techniques. This shows that we can accurately control the chamber temperature via electrical signals in a way that is robust—largely independent of external conditions. The close relation between heater/sensor and chamber is independent of variables at the chip-to-world interface and as a result, if the TCR of the metal film is known within 1%, the chamber temperature can be estimated to within an uncertainty of ± 0.73 C—an uncertainty that is sufficiently small to enable many molecular biology protocols. Together, these enable direct and inexpensive electrical control of the device temperature. As long as the TCR and other fabrication parameters are tightly controlled to ensure repeatable devices, the need for per-device-level calibration can be removed. In closed-loop control, such repeatable devices can compensate for any remaining effect of fluctuations in external variables, becoming highly robust. Reliable operation can then be expected, regardless of changing airflow rate or ambient temperature, as well as packaging variability and chip-to-world gantry/interface materials and configuration. As an example of this robustness, if we were to use a temperature controller to hold T_h constant and allow 10 C variations in both the heat sink temperature (T_{hs}) and air temperature (T_a), the chamber temperature (T_c) would vary by less than 0.4 C. The major determinant of the robustness is the β factor, as summarised in table 2. This is a small enough correction factor that it could be neglected, even for the most demanding of the PCR stages (i.e. annealing). If this correction is made then we might expect to have a temperature uncertainty of 0.1 C.

Simulations indicate that the spatial uniformity is better than approximately ± 1.25 C at any temperature up to 95 C. The actual measurement of the uniformity via fluorescence indicates an even better uniformity of ± 0.65 C, albeit at about half the temperature. Although either variation is adequate for reliable PCRs (in our experience), the slightly better spatial uniformity as deduced from the fluorescence measurements may simply be due to the signal averaging (over 200 points) suppressing the variation.

We also note that if the heater radius were halved, then we would expect (since the power is approximately proportional to r^{-2}) the power consumption would be about 1 W and several chambers could easily fit on a standard CMOS die.

The importance of being able to make an electrical determination of the temperature in a robust design is also shown here. Although the optical method was effective, it required much more equipment and extensive calibration measurements during the experiment (e.g. the fluorescence measurements before and after each heating cycle), as well as in separate experiments (i.e. the calibration curves). By contrast, the

electrical determination of the temperature depended only upon the TCR and the room temperature resistance, both of which are typically defined to tight tolerances within a commercial manufacturing process. In a non-commercial process, these numbers could be determined on a batch-to-batch basis. With those two predetermined parameters the temperature can be robustly controlled using only software and electricity.

5. Conclusions

We have presented an integrated lab-on-chip heater design for which we have been able to show that the chamber temperature is known accurately, as verified optically and electrically. In addition, when the heater is held at a constant temperature, the chamber temperature is not strongly affected by any external variables. With several such chambers, a CMOS die could implement a genetic diagnostic that simultaneously tested for specific sequences on an unknown sample as well as known positive and negative samples. With such a level of integration there would be a compelling argument for the adoption of lab-on-chip devices in healthcare.

In past work we have demonstrated approaches to lab-on-chip procedures that can be scaled to photopolymer/CMOS implementation, with demonstrations of high voltage subsystems [18], optical detection [31], thermal control [21] and microfluidics [20], as well as mm-scale electrophoresis [32]. With the present work we show that this KMPR-based thermal control can be both robust and manufacturable. To our knowledge, this is the first demonstration of a thermally robust, CMOS-compatible design for thermal control without the need for device-level calibration—a key requirement for any inexpensive point-of-care diagnostic. We believe that we are now nearing the point at which entire protocols could be implemented upon CMOS.

Acknowledgments

We gratefully acknowledge the support of Natural Sciences and Engineering Research Canada (NSERC) and Teledyne-DALSA Semiconductor. We also would like to thank S Martel for his helpful discussions and assistance.

References

- [1] Jain A and Goodson K E 2011 *J. Therm. Biol.* **36** 209–18
- [2] Ahmad F and Hashsham S A 2012 *Anal. Chim. Acta* **733** 1–5
- [3] Saha H and Chaudhuri C R 2009 *Def. Sci. J.* **59** 557–67
- [4] Burns M A et al 1998 *Science* **282** 484–7
- [5] Baltes H, Paul O and Brand O 1998 *Proc. IEEE* **86** 1660–78
- [6] Lao A I K, Lee T M H, Hsing I M and Ip N Y 2000 *Sensors Actuators* **84** 11–7
- [7] Lee D S, Park S H, Yang H S, Chung K H, Yoon T H, Kim S J, Kim K and Kim Y T 2004 *Lab Chip* **4** 401–7
- [8] Daniel J H, Iqbal S, Millington R B, Moore D F, Lowe C R, Leslie D L, Lee M A and Pearce M J 1998 *Sensors Actuators* **71** 81–8
- [9] Hoang V N, Kaigala G V, Atrazhev A, Pilarski L M and Backhouse C J 2008 *Electrophoresis* **29** 4684–94

- [10] Selva B, Mary P and Jullien M C 2010 *Microfluid. Nanofluid.* **8** 755–65
- [11] Furuhashi M et al 2013 *Appl. Phys. Lett.* **103** 023112
- [12] Falconi C 2013 *Sensors Actuators* **179** 336–46
- [13] Jung W, Kim Y W, Yim D and Yoo J Y 2011 *Sensors Actuators* **171** 228–32
- [14] Kaigala G V, Hoang V N, Stickel A, Lauzon J, Manage D, Pilarski L M and Backhouse C J 2008 *Analyst* **133** 331–8
- [15] Kaigala G V, Behnam M, Bidulock A C E, Bargaen C, Johnstone R W, Elliott D G and Backhouse C J 2010 *Analyst* **135** 1606–17
- [16] Ma T, Northrup V, Funga A O, Glerum D M and Backhouse C J 2012 *Proc. SPIE* **8412** 84120B–1
- [17] Kaigala G V, Hoang V N and Backhouse C J 2008 *Lab Chip: Miniaturisation Chem. Biol.* **8** 1071–8
- [18] Behnam M, Kaigala G V, Khorasani M, Marshall P, Backhouse C J and Elliott D G 2008 *Lab Chip: Miniaturisation Chem. Biol.* **8** 1524–9
- [19] Behnam M, Kaigala G V, Khorasani M, Martel S, Elliott D G and Backhouse C J 2010 *IET Nanobiotechnol.* **4** 91–101
- [20] Gutierrez-Rivera L, Martinez-Quijada J, Johnstone R, Elliott D, Backhouse C and Sameoto D 2012 *J. Micromech. Microeng.* **22** 085018
- [21] Martinez-Quijada J, Caverhill-Godkewitsch S, Reynolds M, Gutierrez-Rivera L, Johnstone R W, Elliott D G, Sameoto D and Backhouse C J 2013 *Sensors Actuators* **193** 170–81
- [22] Grover W H, Skelley A M, Liu C N, Lagally E T and Mathies R A 2003 *Sensors Actuators* **89** 315–23
- [23] Lienhard J H (V) and Lienhard J H (IV) 2011 *A Heat Transfer Textbook* (Mineola, NY: Dover)
- [24] Convert L, Aimez V, Charette P and Lecomte R 2008 *IEEE 1st Microsystems and Nanoelectronics Research Conf. (15 October, Ottawa)* pp 105–8
- [25] Reynolds M, Elias A, Elliott D G, Backhouse C and Sameoto D 2012 *J. Micromech. Microeng.* **22** 125023
- [26] Fontes J 2005 Temperature sensors *Sensor Technology Handbook* ed J Wilson (Amsterdam: Elsevier) pp 531–61
- [27] Khalifa A J N 2001 *Energy Conversion and Management* **42** 491–504
- [28] Weste N H E and Harris D F 2005 *CMOS VLSI design: a Circuits and Systems Perspective* (Boston, MA: Pearson)
- [29] Ross D, Gaitan M and Locascio L E 2001 *Anal. Chem.* **73** 4117–23
- [30] Abramoff M, Magalhaes P and Ram S 2004 *Biophoton. Int.* **11** 36–42
- [31] Hall G H, Sloan D L, Ma T, Couse M H, Martel S, Elliott D G, Glerum D M and Backhouse C J 2014 *J. Chromatogr. A* **1349** 122–8
- [32] Manage D P, Elliott D G and Backhouse C J 2012 *Electrophoresis* **33** 3213–21